The Ferroelectric-Gate Fin Microwave Acoustic Spectral Processor

Faysal Hakim, Nicholas G. Rudawski, Troy Tharpe, Roozbeh Tabrizian*

Department of Electrical and Computer Engineering, Herbert Wertheim College of Engineering,
University of Florida, Gainesville, FL 32611, USA

Abstract

Wireless communication through dynamic spectrum allocation over microwave bands, essential to accommodate exponentially growing data traffic, requires massive array of radio-frequency (RF) filters for adaptive signal shaping at arbitrary frequencies. However, conventional RF filters based on planar acoustic resonators are incapable of realizing such massive integrated arrays, due to their large footprint and limited on-chip frequency scalability or intrinsic configurability. Here, we present a spectral processor enabled by integration of three-dimensional ferroelectric-gate fin (FGF) nano-acoustic resonators with extreme frequency tailorability, large-scale and dense integrability, and intrinsic switchability. FGFs are created by growing atomic-layered ferroelectric hafnia-zirconia transducers on silicon nano-fins, operate in bulk acoustic modes with lithographically scalable frequencies over 3-28 GHz, and provide record-high frequency – quality factor – electromechanical coupling product ($f \times Q \times k_t^2$) of 19.4×10^{10} (at ~11GHz). Further, they benefit from voltage-controlled tunability of gate-transducer polarization that enables their intrinsic configurability without the need for external switches. A monolithic filter-array, created by electrical coupling of FGFs implemented on a single die is demonstrated covering 9-12 GHz and providing dynamic configurability of the active passband with an isolation as large as 17dB. This demonstration highlights the potential of FGF resonators to realize chip-scale adaptive processors and wideband switch-free multiplexers extendable to millimeter-wave frequencies.

*Corresponding Author. Email: rtabrizian@ece.ufl.edu

Main

Wireless systems rely on numerous preset bands in radio-frequency (RF) spectrum to simultaneously communicate exabytes of data for different applications and among billions of users, with minimum latency and interference[1-3]. The spectrum management of such massive traffic is enabled by a large set of static RF filters, corresponding to preset communication bands, that are orchestrated through a set of switches at the front-end of wireless systems[4-6]. Currently, mobile systems rely on more than a hundred of static filters for RF spectral processing over 0.3 GHz – 7 GHz[7-9]. These filters are created from electrical coupling of surface and bulk acoustic wave (SAW and BAW) resonators, to benefit from their small size compared to electrical and optical counterparts, which is due to the significantly lower acoustic wave velocity compared to electromagnetic waves. SAW and BAW filters with different frequencies and bandwidths are packaged in various chips and heterogeneously integrated with lumped-element passives and RF switches to form multi-band spectral processors in RF front-end circuitry.

However, the current spectral processing architecture based on static filtering is not scalable with exponential increase in wireless users, due to emergence of the internet of things, as well as progressive demand for higher data rates and bandwidths in new applications such as the metaverse. To accommodate this ever-growing data traffic, new wireless generations target the use of dynamic spectrum allocation, instead of relying on static bands, to substantially enhance the spectrum-use efficiency[10-12]. Dynamic spectrum allocation requires highly adaptive spectral processors that provide extensive configurability of filter type, frequency, and bandwidth, over a large microwave spectrum stretching to the millimeter-wave regime.

A widely adaptive microwave spectral processor requires a resonator technology that either provides extensive tunability, to cover a wide spectrum of interest using one or few elements, or enables massive arraying and extreme frequency scalability in a reasonable integrated footprint[13-15]. This cannot be implemented using conventional piezoelectric SAW and BAW resonators, since they suffer from at least two of the following deficiencies.

First, they provide little to no intrinsic frequency tunability, limited to few percent[16-19], at the acoustic component level, which is not sufficient to create a configurable filter that covers a wide spectrum. Further, commercially available BAW resonators and filters are implemented in non-ferroelectric materials (*e.g.*, aluminum nitride (AlN)) that do not provide any means for intrinsic switchability required for massive arraying. A solution to this deficiency is being explored by using scandium-aluminum nitride (AlScN), instead of AlN, that provides ferroelectric behavior[20-25]. However, the very large coercive field of AlScN, along with the few hundreds of nanometer thickness of the film required for creation of ultra- and super-high-frequency BAW resonators, results in very large switching voltages, exceeding 100V, that are not readily available on the chip. These limitations may be addressed by integrating off-chip tunable passives or RF switches[26-28], but generally at the cost of degraded performance, excessive footprint and power consumption, and integration challenges.

Second, they offer limited lithographical frequency tailorability, which hinders monolithic integration of multi-band filter arrays on the same chip and within the same fabrication process. Third, their planar architecture inherently limits massive arraying as it imposes excessive footprint consumption and makes large-scale and dense integration challenging.

In this work, we demonstrate the use of the third geometrical dimension to create non-planar acoustic resonators that surpass fundamental limits of planar counterparts for massive arraying and frequency scaling. Similar to non-planar transistors (*i.e.*, fin field effect transistors), extending the functional volume of acoustic resonators to the third dimension enables substantial enhancement in integration density without reducing interface area (*i.e.*, electromechanical transduction area). Further, the three-dimensional resonator structure benefits from new acoustic resonance modes that offer lithographical frequency tailorability independent from piezoelectric film thickness[29], which is constant across the wafer and limits scaling of conventional BAW resonators[30, 31].

The presented resonators are based on high-aspect-ratio silicon (Si) nano-fins that are wrapped around by an atomic-layered hafnia-zirconia ($Hf_{0.5}Zr_{0.5}O_2$, or simply HZO) ferroelectric-gate that serves for piezoelectric transduction. The unique ferroelectric HZO gate transducer, not only benefit from conformal growth on the sidewall of fin, which is essential for transduction of the three-dimensional resonator, but also provides voltage-tunable polarization that enables intrinsic switching of the resonators using temporary application of a dc bias[32-34]. The resulting ferroelectric-gate fin (FGF) architecture enables excitation of intrinsically switchable lateral-BAW modes with a frequency that is defined lithographically by nano-fin width; hence, enabling dense integration of configurable resonator arrays covering a wide spectrum, on a single chip and without the need for external switches. The FGF nano-acoustic resonators serve as building blocks to provide poles and zeros at arbitrary frequencies, thus facilitating realization of highly adaptive microwave spectral processors for modern wideband dynamic wireless systems.

In this paper, an implementation process for intrinsically switchable FGF resonators and filters is presented that enables tight control required for repeatable batch-fabrication of fins with frequencies over a wide spectrum. This, along with an analytical node-scaling model presented in this paper highlights a path for creation of FGF's process design kit that is essential for flexible co-design of acoustic processors and analog circuity to create adaptive RF front-end systems. FGF nano-acoustic resonators over 3-27 GHz with frequency-quality factors ($f \times Q$) as high as 0.76×10^{13} and electromechanical coupling – quality factor product ($k_t^2 \times Q$) as large as 17.7 are demonstrated and their intrinsic switchability using ~44V dc voltage is shown. FGF resonators with different fin widths are electrically coupled on the chip to create configurable bandpass filter arrays with arbitrary center-frequency and bandwidth over 9-12 GHz, highlighting the capability of FGFs to create chip-scale switch-free adaptive microwave spectral processors for dynamic spectrum use.

FGF Nano-Acoustic Resonator Concept and Scaling

FGF nano-acoustic resonators are created by conformal covering of a high-aspect-ratio semiconductor rectangular parallelopiped with a piezoelectric transducer. Such a structure enables excitation of various harmonics of width-extensional BAW modes (*i.e.*, $\mathrm{WE_n}$, $n \in \mathbb{N}$), created from propagation of planar waves in the width direction and reflection at the stress-free surfaces on the two sides. The conformal transducer is composed of a piezoelectric film sandwiched between two metal electrodes that enable application of electric-field across for electromechanical excitation of acoustic waves and mechanical resonance modes. To achieve efficient transduction of $\mathrm{WE_n}$ modes, the piezoelectric film is required to have a polar axis perpendicular to the sidewall of fin. Further, when the polar axis of transducers on both sidewalls are aligned either inward or outward, the excitable modes are limited to odd harmonics (*i.e.*, $n = 2k + 1, k \in \mathbb{Z}$).

FGF resonators benefit from a large transduction area that is scalable by fin height as well as number of fins that are closely packed and electrically coupled. Figure 1 (a) shows the schematic of a one-port FGF resonator composed of three parallel fins with the same dimensions. In this architecture, two ferroelectric-gates (*i.e.*, RF terminals) are placed across the fins and electrically coupled through floating bottom electrodes covering each fin. The floating electrode enables extension of the applied electric field in transducer, resulting in higher electromechanical coupling and improved resonator admittance[35]. Figure 1 (a) inset shows the proposed symbol for the one-port FGF resonator created from three fins. Figure 1 (b) shows the cross-sectional mode-shapes of $WE_{1,3,5}$ modes in electroded area, simulated using COMSOL while exciting the resonator at its resonance frequency using electric field application between top electrodes. The mode shapes correspond to an FGF with Si fin width (W_{fin}) of 500nm, HZO piezoelectric film thickness (T_{HZO}) of 100nm, and tungsten (W) electrode thickness of 50nm. As evident in the mode shapes, the energy of WE_n modes are localized in the fin volume, with minimum leakage to the supporting substrate that is mimicked using low-reflectivity boundary condition under fin anchor. Further, except for the top and bottom of the fin, the mechanical stress field is uniform over the entire height of the fin, enabling efficient piezoelectric coupling of BAW modes with minimum charge cancellation.

The frequency of WE_n modes (f) in FGF resonators is defined by the path of BAW as propagating across the resonator width, consisting of semiconductor fin width as well as the ferroelectric gate and metal electrode thicknesses. Therefore, f can be lithographically scaled by changing the fin width. Considering the variation of longitudinal acoustic wave velocity in different materials across resonator width, the frequency scaling with W_{fin} does not follow a simple closed-form expression. In this work, Mason's waveguide modeling approach is used to predict performance metrics of WE_n modes for different W_{fin} and T_{HZO}, and based on fundamental material properties. In this model, each constituent layer across resonator width is represented by frequency-dependent lumped electrical impedances that represent equivalent mass, stiffness, and damping as well as electromechanical transduction (in piezoelectric layers). This simplifies the FGF nano-acoustic resonator to an equivalent circuit network, enabling prediction of resonator admittance, and extraction of frequency, Q, and k_t^2 of all WE_n harmonics (see Supporting Information, section S1, for detailed discussion on the modeling approach). It is worth noting, in this approach the resonator is modeled as a multi-layer waveguide created from plates of different materials (*i.e.*, Si, HZO, metal). This corresponds to an infinitely tall FGF (*i.e.*, no mechanical boundaries at the two ends in fin-height direction) that is subjected to longitudinal plane waves that induce WE_n modes. Therefore, while the frequency scaling plot is very close to the practical case of an FGF with finite height, the Q and k_t^2 scaling plots present the upper limits. In practice, Q and k_t^2 values will be lower due to material imperfections and various energy loss mechanisms, such as thermoelastic dissipation and acoustic energy leakage to the substate, that are not captured in the waveguide-based model.

Figure 1 (c) shows the scaling plots for WE_3 mode, which is the mode used for implementation of filters, as a function of W_{fin} and for different T_{HZO}. In frequency scaling plot, two regions with different characteristics are identified. In the first region where fin-width is significantly larger compared to transducer thickness, the frequency is scaled inversely linear with W_{fin}. In the second region corresponding to narrower fins and higher frequencies, frequency scaling deviates from inversely linear relation. This corresponds to an increased effect of acoustic-impedance mismatch between Si and HZO with W at small BAW wavelengths, resulting in large reflection of the wave at material boundaries, which translates to a smaller effective paths and higher frequencies. Further, it is evident that extreme frequency scaling to mm-wave regime requires reduction in HZO thickness to 20nm. This is perfectly feasible considering extreme thickness scalability of HZO films to few nanometers while sustaining a large polarization and piezoelectric coupling[32, 36]. Figure 1 (c) also shows the scaling characteristics for k_t^2 and Q limits in nano-fin resonators with different W_{fin} and T_{HZO}, highlighting an opposite trend. k_t^2 limit increases with relative reduction of W_{fin} to T_{HZO}, as a result of relative increase in the volume of electromechanically active (*i.e.*, piezoelectric) material in resonator structure. On the other hand, resonator Q limit reduces with relative reduction of W_{fin} to T_{HZO}, corresponding to the higher acoustic energy dissipation rate in polycrystalline HZO film compared to single-crystal Si fin[37-39]. Single-crystal silicon fin not only enhances the Q of FGF, when compared to HZO BAW and Lamb-wave counterparts[34, 40], but also enhances the power handing of the device by extending the linear elastic range[41, 42] and serving as a heat sink to the substrate (*i.e.*, similar to solidly mounted BAW counterparts[43]).

FGF resonators can be intrinsically switched between "On" and "Off" states, through depolarization of the ferroelectric gate via application of dc or low-frequency voltage pulses over a short period of time. The switching voltage depends on the ferroelectric gate thickness and HZO coercive field, at which transducer polarization and piezoelectric coupling are nulled. Once the device is switched off, it configures into a static capacitor without any resonance peaks. The FGF can be switched back to the "On" state by application of polling field, that is typically 1.5 times higher than the coercive field[42, 44].

FGF Nano-Acoustic Resonator Implementation and Characterization

The performance of an FGF resonator correlates closely with its three-dimensional geometry as well as mechanical, electrical, and electromechanical properties of constituent materials. First, efficient excitation of BAW modes with uniform energy distribution and minimum charge cancellation, essential for linear operation and high k_t^2, requires a constant fin width and transducer thickness across the entire height. This becomes excessively challenging when increasing the aspect-ratio of fins to enhance their transduction area and reduce resonator impedance. Second, the interfaces of constituent layers in nano-fin resonator should be as smooth as possible to minimize surface scattering of BAW that degrades resonator Q[44-46]. This is especially crucial when targeting an increase in frequency that corresponds to reduced BAW wavelength and higher surface scattering. Third, efficient electromechanical transduction for high k_t^2 requires accurate control over the crystallinity and polarity of piezoelectric film grown on the sidewall. This is highly challenging as conventional piezoelectric film-growth techniques are optimized for high quality planar films[47, 48]. In these techniques, films grown on non-planar surfaces have poor texture and crystallinity, or polar-axis misorientation from surface normal[49]. Forth, as an inherently three-dimensional device, creation of FGF resonators require dimensionally selective patterning of metal electrodes to form well-defined RF terminals with reduced static electrical feedthrough.

In this work, a fabrication process is developed to realize stringent geometrical and material requirements, as well as three-dimensional electrode patterning, to create high-performance FGF nano-acoustic resonators and filters. The fabrication process consists of three key steps. First, Si fins with ultra-high aspect-ratios are created by chemical etching with crystallographic selectivity. The fins are created on (110) silicon-on-insulator substrates, and are aligned to [112] crystallographic direction. When exposed to basic wet etchants (*e.g.*, potassium hydroxide, tetramethylammonium hydroxide), such crystallographic alignment enables formation of rectangular parallelopipeds with perfectly straight sidewalls, due to the near-perfect etch stop at [111] planes. This approach not only enables creation of ultra-high aspect-ratio fins with constant width across the height, but also yield ultra-smooth Si sidewall surfaces. Further, benefiting from crystal-based chemical reaction, very consistent fin widths can be achieved, which is essential for batch fabrication of FGFs with consistent operation. See Supporting Information, section S2, for SEM image of fin arrays highlighting the consistent control over fin widths after chemical etching.

Second, the FGF nano- acoustic resonators of this work benefit from ferroelectric transducer that is entirely grown using conformal atomic layer deposition (ALD). The centerpiece of the transducer, *i.e.*, the ferroelectric film with large piezoelectricity and intrinsic polarization switchability, is created from formation of HZO superlattice created by periodic stacking with alumina (Al_2O_3) interlayers. HZO superlattice is recently demonstrated as a hence piezoelectric transducer with large electromechanical transduction, high acoustic velocity, and low energy dissipation[37, 50-52]. The conformal ALD growth enables achieving ferroelectric-gate transducers with uniform thickness, texture, crystallinity, and polarization over the entire sidewall of Si fins. This, along with capability of creating fins with consistent and controllable widths across the wafer, is crucial for creation of batch-manufacturable FGF spectral processors on large substrates. Further, atomic-layered ferroelectric HZO film have shown exceptional preservation of their polarization and piezoelectricity even when scaled to few nanometers. These make HZO superlattice an ideal choice for creation of FGF nano- acoustic resonators with extreme frequency scalability to mm-wave regime. In this work, HZO superlattice with thickness of 100nm (*i.e.*, ten 9nm-thick HZO layers laminated with nine 1nm-thick Al_2O_3 interlayers) is sandwiched between 50nm-thick W electrodes that are also deposited using ALD.

Finally, the three-dimensional bottom and top W electrode are patterned using anisotropic and isotropic dry etching, respectively. High dimensional selectively is achieved by using photoresist masks with large aspect-ratio. Detailed information on chemicals and techniques used for fabrication of FGF nano-acoustic resonators and filters, as well as the process flow schematic, are presented in Supporting Information, section S2.

Figure 2 (a, b, c) shows the scanning electron microscope (SEM) images of FGF resonators formed from a single or multiple fins, from different angles. For the multi-fin structure, the continuity of top electrodes (*i.e.*, three-dimensional gates) over the five fins is captured by top-view SEM image. Also, the three-dimensional profile of the top electrode is evident in side-view SEM images. Figure 2 (c, d) shows cross-sectional high-angle annular dark-field scanning transmission electron microscope (HAADF-STEM) images of FGF resonators cross-section, for devices with different Si fin widths of 186nm and 707nm, and fin height of ~6300nm. The very large aspect ratios, as high as 34:1, while having a perfectly straight and smooth Si sidewall, is evident in images. Figure 2 (c, d) also shows images zoomed on top and bottom corners of the resonators. These images show the perfectly isolated bottom W electrodes that only exist on the sidewalls, the conformal HZO superlattice transducer, and the conform top W electrodes. Figure 2 (e, f) shows a high-resolution TEM image zoomed on the HZO superlattice, highlighting the constituent layers as well as polar orthorhombic texture and c-axis orientation in grains of two different HZO layers.

FGF resonators with Si fin width ranging from 300nm to 1000nm are implemented and their performance is characterized using RF electrical measurements. Prior to RF characterization, HZO transducer is poled, through application of 1kHz bipolar pulses, to enhance linear transduction with large longitudinal piezoelectric coefficient (*i.e.*, d_{33})[52, 53]. See Supporting Information, section S3, for detailed discussion on transducer poling. Following transducer poling, one-port FGF resonators are characterized by measuring their reflection coefficient (*i.e.*, S_{11}), when excited with -5dBm input power. Resonator admittance is extracted from S_{11} response. The performance merits of resonators are evaluated by extracting the Q of series resonance peak and electromechanical coupling k_t^2, using standard approaches[54, 55], from the measured admittances.

Figure 3 (a) shows the measured admittance of FGF resonators with 300nm and 1000nm Si fin widths, over a wide frequency span, highlighting excitation of different WE harmonics. For the FGF with 1000nm Si fin width, WE_3 and WE_5 modes are evident at 8.55 GHz and 11.86 GHz, respectively. For the resonator with 300nm Si fin width, WE_1, WE_3, and WE_5 modes are evident at 3.07 GHz, 11.61 GHz, and 27.29 GHz, respectively. Figure 3 (b) shows the measured admittance of FGF resonators around WE_3 mode, for different Si fins over 300nm to 1000nm range, all implemented in the same batch. The frequency scaling of WE_3 mode frequency over 9-12 GHz with fin widths changing over 300nm to 1000nm is observed. The highest k_t^2, with a value of 4.94%, is measured for FGF at 11.27 GHz. The highest Q, with a value of 816, is measured for the FGF at 8.55 GHz. Besides the targeted WE_3 mode, lower and higher harmonics are also characterized to evaluate performance over extreme frequency extension in super-high frequency (SHF) regime. Figure 3 (c) shows the measured admittance of selective WE_1 and WE_5 peaks over 3-30 GHz for FGF resonators with different fin widths. The highest Q, with a vaule of 1148, is extracted from the WE_1 mode of the FGF resonator with W_{fin} of 300nm. In this resonator, we have also measured the highest frequency peak, standing noticeably out of the feedthrough level, at 27.2 GHz, showing a Q of 77 and k_t^2 of 0.27%. In summary, the highest frequency-Q product ($f \times Q$) of 0.76×10^{13} is measured for the resonator with 500nm fin width at 18.78 GHz (WE_5 mode), and the highest $k_t^2 \times Q$ of 17.73 is measured for the resonator with 500nm fin width at 10.96 GHz (WE_3 mode). See Supporting Information, section S4, for detailed performance merits of WE modes for resonators with different fin widths. Also, see the Supporting Information, section S5, for the plot that summarizes $k_t^2.Q$ figure of merit for all WE_n peaks presented in Fig. 3 (c, d), in comparison with published data from planar BAW resonators, over SHF spectrum.

The FGF resonators are characterized for their intrinsic switchability by temporary application of dc bias voltage between top electrodes, through a bias-Tee. Figure 3 (d) shows the measured polarization hysteresis loop for an arbitrary FGF resonator of this batch, where the value of bias voltages applied to two FGF resonators with different frequencies are highlighted. The resonators are measured in three states. The On state corresponds to unbiased operation, assuming a poled resonator. The Off state correspond to an applied bias of ~44V dc, where the net polarization is nulled. The depolarized state correspond to intermediate states where the bias is between 0V and 44V dc. The switching experiment is applied to FGFs with W_{fin} of 300nm and 500nm that are initially polled in up and down polarization states of ferroelectric gate, respectively. The transformation of resonator admittances upon changing dc bias voltage is evident. Specifically, in the Off state, the resonator is configured into a static capacitor where no resonance and antiresonance peaks are discernible.

FGF Nano-Acoustic Filter Array

FGF resonators are electrically coupled to form bandpass filters. Resonators with different fin width are connected through planar routings to form 2.5-stage ladder filters. An array of filters is implemented with lithographically tailorable center-frequency and bandwidth, to realize a spectral processor for dynamic spectrum control over 9-12 GHz. Figure 4 shows SEM images of an FGF filter from different angles. The filter is created from three series resonators and two shunt resonators, electrically connected to form the 2.5-stage ladder. The frequency and transduction area of series and shunt resonators in the ladder are optimized for proper passband impedance matching and isolation, needed for high-selectivity shape-factors[56]. This include optimizing Si fin widths to overlap the parallel resonance of shunt resonator with series resonance of series resonator in ladder filter. The transduction area of shunt resonators are also optimized to be nearly twice that of series, by changing corresponding gate widths, to ensure large out of band rejection. It is worth noting, thanks to the use of the third dimension for scaling resonator admittance, densely integrated

FGF filter arrays can be realized for coverage of a wide spectrum. See Supporting Information, section S6 for an example of densely FGF integrated filter arrays where fifty six 2.5-stage ladder filters are fitted, along with trimming inductors, on a 400μm×400μm planar footprint.

Figure 5 shows the measured transmission responses magnitude ($|S_{21}|$), with 50Ω terminations, for FGF filters with different frequencies over 9-12 GHz, created from resonators with different fin widths. The change in filter bandwidth at different center-frequencies corresponds to the change in k_t^2 with the scaling of Si fin width. It is worth noting, the inconsistent k_t^2 and Q of co-fabricated FGFs with frequencies scaled over a wide spectrum prevents creation of ladder or lattice acoustic filters that provide similar fractional bandwidth (FBW). However, in some applications, such as densely integrated active electronically scanned arrays used in phased array radars, achieving full coverage of a wide spectrum with configurable single-chip spectrum analyzer is the first priority, independent from FBW consistency of constituent filters. Also, FBW inconsistency over frequency scaling can be addressed by opting for more complex architectures and through exploiting lumped element passives[57, 58], at the cost of design and integration complexity and footprint overhead.

The filters are intrinsically switched through temporary application of dc voltage between signal and ground at the two ports. Biases as large as 63V is applied through bias-Tee, inducing a ~44V on each of series resonators in the first and last stage, to switching them off. This configuration enables intrinsic switching of all resonators in the 2.5-stage filter, except the series resonator at the ladder center. Therefore, the Off state of the filter still shows a notion of passband that reduces isolation. This can be avoided by embedding switching ports at the center of the ladder to access all the resonators for intrinsic switching. The transmission response of the filters in Off state is shown in Fig. 5, in comparison with the On state response, highlighting passband isolation while the out-of-band rejection remains nearly the same. This is due to the nature of intrinsic switching in FGF, where upon switching only the motional branch of the resonator is opened while shunt capacitance corresponding to dielectricity of depolarized gate remains. The detailed performance merits of filters in fig. 5 are presented in Supporting Information, section S7.

In all the filters, large ripples are evident over the passband, as a result of spurious modes in resonator admittances that correspond to Lamb waves propagating in height or length direction of the fin. These spurs may be suppressed by proper dispersion engineering through opting for geometrical variations in Si fin across its height and length[59, 60]. Further, the large insertion-loss of filters can be reduced by opting for multi-fin resonator architecture, to scale the admittances for proper matching with 50Ω electrical terminations, as well as further densification of arraying to reduce excessive loss due to planar routing lines.

The presented intrinsically switchable FGF filters can be used for creation of a switch-free single-chip multiplexer for configurable spectral processing at the RF front-end. The multiplexer can be realized by placing intrinsically switchable FGF filters in parallel. In this configuration, the active filter can be selected by switching all other filters into the Off state. However, the impedance loading of these Off filters on the On filter degrades the performance. This can be suppressed by adding a matching circuit, consisting of passive elements, in parallel with filters. See Supporting Information, section S8, where this concept is explored by identifying the required passive circuit network to achieve a fully configurable switch-free multiplexer with a performance consistent with isolated filters shown in Fig. 5. This demonstration highlights the potential of FGF technology to create single-chip configurable wideband spectral processors.

Conclusion

We have reported a three-dimensional nano-acoustic resonator technology that enables large-scale integration of RF filters with lithographically defined performance, to enable realization of single-chip switch-free dynamic spectral processors with extreme frequency scalability. The resonators are created by covering high aspect-ratio Si fins with atomic-layered ferroelectric HZO transducer gates. These ferroelectric-gate fin (FGF) nano-acoustic resonators operate in lateral BAW modes with frequency, Q, and k_t^2 scalable lithographically by Si fin width as well as transducer thickness over cm- and mm-wave regimes. Further, FGF resonators benefit from intrinsic switchability provided by ferroelectric behavior of gate transducer. A waveguide-based analysis is presented to accurately predict scaling characteristic of FGF resonators and enable proper filter design. The fabrication process developed for creation of FGF resonators, consisting of crystallography dependent chemical etching and atomic layer deposition techniques to realize fin structures with ultra-high aspect-ratio and straight and smooth sidewalls, and conformal piezoelectric transducers with uniform thickness and acoustic properties over the fin sidewalls. Intrinsically switchable FGF resonators with frequencies over 3-27 GHz are demonstrated with $f \times Q$s as high as 0.76×10^{13} and $k_t^2 \times Q$s as high as 17.73. FGF resonators different fin-widths are electrically coupled to form bandpass intrinsically switchable filter arrays with lithographically defined center-frequency and bandwidth, covering 9-12 GHz. The presented microwave acoustic resonator technology shows a promising perspective for realization of a chip-scale widely adaptive switch-free spectral processors for dynamic spectrum allocation in future wireless systems.

Methods

Wafer specification: For fabrication of nano fins, silicon-on-insulator (SOI) wafers are used. For crystallographic orientation dependent etching of fins, a 6μm-thick (110)-oriented device layer with <110> orientation and <112> primary flats is used. The buried oxide (Box) and handle layer thicknesses are 500nm and 500μm respectively. The handle layer had a resistivity exceeding 10,000 ohm.cm to reduce the effect of substrate feedthrough.

Film deposition:

ALD of $Hf_{0.5}Zr_{0.5}O_2 – Al_2O_3$ superlattice: Amorphous $Hf_{0.5}Zr_{0.5}O_2$ - Al_2O_3 superlattice transducers are deposited using a Cambridge NanoTech Fiji 200 atomic layer deposition system with a process setpoint of 200°C. 9.2nm-thick layers of $Hf_{0.5}Zr_{0.5}O_2$ are deposited using 56 cycles of tetrakis(dimethylamido)hafnium(IV) (TDMAH) and tetrakis(dimethylamido)zirconium(IV) (TDMAZ) precursors pulsed with a 1:1 ratio. 300W hydrogen and oxygen plasmas are applied following each monolayer deposition for precursor oxidation with enhanced orthorhombic phase concentration34. Next, 1nm-thick Al_2O_3 is thermally deposited using 10 cycles of trimethylaluminum (TMA) precursor to limit $Hf_{0.5}Zr_{0.5}O_2$ vertical grain size to sub-10nm, during further deposition steps. This 9.2nm $Hf_{0.5}Zr_{0.5}O_2$ – 1nm Al_2O_3 deposition sub-cycle is then repeated additional times (depending on targeted thickness), followed by a final 9.2nm deposition of $Hf_{0.5}Zr_{0.5}O_2$.

ALD of W electrode: Amorphous W electrodes are deposited in ALD chamber using silane (SiH_4) and tungsten hexafluoride (WF_6) gas.

Device fabrication: Supporting Information Fig. S2 depicts the three-mask fabrication process flow used to implement nano-fin acoustic resonators. First, 200nm silicon oxide (SiO_2) is patterned on SOI wafer via optical lithography to serve as hard mask for fin etching. Then, the sample is submerged in 2.3% tetra methyl ammonium hydroxide (TMAH) solution at 65°C for 15 mins to etch 6.5μm silicon and define fins. This is followed by removal of SiO_2 mask in buffered oxide etchant. Next, a 50nm-thick W is deposited using ALD. The deposited W is anisotropically etched in reactive ion etching (RIE) chamber using sulfur hexafluoride (SF_6) and argon (Ar) gas mixture to remove W layer on all planar surfaces, while keeping it on sidewalls of fins. After RIE of W to serve as floating bottom electrode in FGF, a 100nm-thick $Hf_{0.5}Zr_{0.5}O_2 – Al_2O_3$ superlattice is deposited by ALD, followed by another 50nm-thick W layer. Next, the wafer is subjected to rapid thermal annealing (RTA) using SSI Solaris 150 tool for 20s at 500°C in N_2 ambient, to promote preferred morphology in the superlattice film (*i.e.*, polar orthorhombic phase). Then, the top W layer is patterned isotropically in RIE chamber, by SF_6 gas, using 10μm-thick photoresist mask. Finally, 500nm-thick gold (Au) layer is deposited by lift-off to serve for routings and probing pads.

Device characterization:

<u>DC analysis:</u> Polarization – electric field (P-E) hysteresis loop of $W/Hf_{0.5}Zr_{0.5}O_2 – Al_2O_3/W$ sidewall capacitors with different areas are obtained using Radiant PiezoMEMS Analyzer. For this analysis, a 45V, 1 kHz square pulse is applied between the two ports of resonator for 1s to wake the film up. Then, a 70V bipolar (triangular) pulse train at 10 kHz is applied to obtain the P-E loop.

<u>RF measurement and analysis:</u> After cycling and setting DC operating point, the FGF resonators are measured using a Keysight N5222A vector network analyzer with an input power -5 dBm.

SEM imaging: SEM images are taken using FEI Nova NanoSEM 430 tool.

S/TEM imaging:

Sample Preparation: A modified in-situ lift-out process using an FEI Helios G4 CXe dual plasma focused ion beam/scanning electron microscope equipped with a Pt GIS and EasyLift in-situ micromanipulator is used to prepare samples for S/TEM imaging. Electron-beam induced deposition of Pt is used to produce a ~2 μm-thick conformal protective coating on the whole surface of the device. The device is then in-situ lifted out and welded to a Ted Pella Mo lift-out grid such that the tall direction of the fin is aligned to the stage normal direction. The grid is removed from the stage and then ex-situ rotated up to 45 degrees by hand and then reloaded onto the stage for final thinning to electron transparency; this results in the tall direction of the fin being rotated away from the stage normal direction by same amount of ex-situ rotation and, by extension, the FIB milling direction during subsequent final thinning; this is necessary to produce a lamella with the most uniform thickness and minimal curtaining effects to allow accurate inspection of the film quality at all points on the fin surface. Thinning is initially started at 30 kV and then completed at 8 kV to reduce damage layer thickness.

Sample Imaging: An FEI Themis Z scanning/transmission electron microscope (S/TEM) with Cs probe correction, equipped with a Fischione Instruments Model 3000 high-angle annular dark-field (HAADF) STEM detector and FEI Ceta 16 megapixel CMOS camera is used to perform HAADF-STEM and high-resolution (lattice) imaging (HR-TEM).

Data Availability

The authors affirm that the main data supporting the findings of this article are available within the manuscript and its Supporting Information. Extra data are available from the corresponding author upon request.

Acknowledgement

The authors would like to thank Dr. Timothy Hancock for technical discussions and support of this effort, and the University of Florida Nanoscale Research Facility cleanroom staff for fabrication support. F.H., T.T., and R.T. acknowledge the financial support from the Defense Advanced Research Projects Agency (DARPA) through the Young Faculty Award (Grant D19AP00044) and National Science Foundation (NSF) through the CAREER award (Grant ECCS-1752206). The Herbert Wertheim College of Engineering Research Service Centers is acknowledged for use of the FEI Helios G4 CXe dual plasma focused ion beam/scanning electron microscope and FEI Themis Z scanning/transmission electron microscope.

References

1 S. Dang, O. Amin, B. Shihada, M. S. Alouini, What should 6G be?, *Nature Electronics* **3**, 20-29 (2020).

2 S. Borkar, H. Pande, Application of 5G next generation network to Internet of Things, *International Conference on Internet of Things and Applications (IOTA)* **2016**, 443-447.

3 Y. Wang, J. Li, L. Huang, Y. Jing, A. Georgakopoulos, P. Demestichas, 5G Mobile: Spectrum Broadening to Higher-Frequency Bands to Support High Data Rates, *IEEE Vehicular Technology Magazine*, **9**, 39-46 (2014).

4 A. O. Watanabe, M. Ali, S. Y. B. Sayeed, R. R. Tummala, M. R. Pulugurtha, A Review of 5G Front-End Systems Package Integration. *IEEE Transactions on Components, Packaging and Manufacturing Technology*, **11**, 118-133 (2021).

5 S. Mahon, The 5G Effect on RF Filter Technologies. *IEEE Transactions on Semiconductor Manufacturing*, **30**, 494-499 (2017).

6 R. Ruby, A Snapshot in Time: The Future in Filters for Cell Phones, *IEEE Microwave Magazine*, **16**, 46-59 (2015).

7 R. Aigner, G. Fattinger, 3G – 4G – 5G: How Baw Filter Technology Enables a Connected World. *2019 20th International Conference on Solid-State Sensors, Actuators and Microsystems & Eurosensors XXXIII (TRANSDUCERS & EUROSENSORS XXXIII)* **2019**, 523-526.

8 R. Aigner, G. Fattinger, M. Schaefer, K. Karnati, R. Rothemund, F. Dumont, BAW Filters for 5G Bands. *2018 IEEE International Electron Devices Meeting (IEDM)* **2018**, 14.5.1-14.5.4.

9 D. Kim, G. Moreno, F. Bi, M. Winters, R. Houlden, D. Aichele, J. B. Shealy, Wideband 6 GHz RF Filters for Wi-Fi 6E Using a Unique BAW Process and Highly Sc-doped AlN Thin Film, *2021 IEEE MTT-S International Microwave Symposium (IMS)* **2021,** 207-209.

10 W. S. H. M. W. Ahmad, N. A. M. Radzi, F. S. Samidi, A. Ismail, F. Abdullah, M. Z. Jamaludin, M. Zakaria, 5G technology: Towards dynamic spectrum sharing using cognitive radio networks. *IEEE Access*, **8**, 14460-14488 (2020).

11 J. Zhu, K. J. R. Liu, Cognitive radios for dynamic spectrum access-dynamic spectrum sharing: A game theoretical overview, *IEEE Communications Magazine*, **45.5***,* 88-94 (2007).

12 CL. I, S. Han, S. Bian, Energy-efficient 5G for a greener future, *Nature Electronics*, **3**, 182–184 (2020).

13 R. Gómez-García, A. C. Guyette, Reconfigurable Multi-Band Microwave Filters, *IEEE Transactions on Microwave Theory and Techniques*, **63**, 1294-1307 (2015).

14 D. Marpaung, J. Yao, J. Capmany, Integrated microwave photonics. *Nature Photonics,* **13**, 80–90 (2019).

15 J. Fandiño, P. Muñoz, D. Doménech, J. Capmany, A monolithic integrated photonic microwave filter. *Nature Photonics*, **11**, 124–129 (2017).

16 M. Shahmohammadi, D. Dikbas, B. P. Harrington and R. Abdolvand, Passive tuning in lateral-mode thin-film piezoelectric oscillators, *Proceedings of 2011 Joint Conference of the IEEE International Frequency Control and the European Frequency and Time Forum (FCS)*, San Francisco, CA, USA, 2011, pp. 1-5.

17 A. Norouzpour-Shirazi, M. Hodjat-Shamami, R. Tabrizian and F. Ayazi, Dynamic tuning of MEMS resonators via electromechanical feedback, *IEEE Transactions on Ultrasonics, Ferroelectrics, and Frequency Control*, vol. 62, no. 1, pp. 129-137, January 2015.

18 H. Chandrahalim, S. A. Bhave, R. Polcawich, J. Pulskamp, D. Judy, R. Kaul, and M. Dubey, Influence of silicon on quality factor motional impedance and tuning range of PZT-transduced resonators. *Proceedings of 2008 Solid State Sensor, Actuator and Microsystems Workshop*, pp. 360-363, June 2008.

19 S. Dabas, D. Mo, S. Rassay and R. Tabrizian, Intrinsically Tunable Laminated Ferroelectric Scandium Aluminum Nitride Extensional Resonator Based on Local Polarization Switching,

Proceedings of 2022 IEEE 35th International Conference on Micro Electro Mechanical Systems Conference (MEMS), Tokyo, Japan, 2022, pp. 1050-1053.

20 S. Fichtner, N. Wolff, F. Lofink, L. Kienle, and B. Wagner, AlScN: a III–V semiconductor based ferroelectric. *J. Appl. Phys.* **125**, 114103 (2019).

21 J. Wang, M. Park, S. Mertin, T. Pensala, F. Ayazi and A. Ansari, A Film Bulk Acoustic Resonator Based on Ferroelectric Aluminum Scandium Nitride Films, *Journal of Microelectromechanical Systems*, vol. 29, no. 5, pp. 741-747, Oct. 2020.

22 S. Rassay, D. Mo, C. Li, N. Choudhary, C. Forgey and R. Tabrizian, "Intrinsically Switchable Ferroelectric Scandium Aluminum Nitride Lamb-Mode Resonators," *IEEE Electron Device Letters*, vol. 42, no. 7, pp. 1065-1068, July 2021.

23 D. Mo, S. Dabas, S. Rassay and R. Tabrizian, "Complementary-Switchable Dual-Mode SHF Scandium Aluminum Nitride BAW Resonator," in *IEEE Transactions on Electron Devices*, vol. 69, no. 8, pp. 4624-4631, Aug. 2022.

24 V. Gund, K. Nomoto, H. G. Xing, D. Jena and A. Lal, "Intrinsically Switchable GHz Ferroelectric ScAlN SAW Resonators," *2022 IEEE International Symposium on Applications of Ferroelectrics (ISAF)*, Tours, France, 2022, pp. 1-4.

25 D. Mo, S. Rassay, C. Li, and R. Tabrizian, Intrinsically Switchable Dual-Band Scandium-Aluminum Nitride Lamb-Wave Filter, *physica status solidi (RRL)–Rapid Research Letters*, *16*(11), 2200135, 2022.

26 H. Hirano, T. Samoto, T. Kimura, M. Inaba, K. -y Hashimoto, T. Matsumura, K. Hikichi, M. Kadota, M. Esashi, S. Tanaka, Bandwidth-tunable SAW filter based on wafer-level transfer-integration of $BaSrTiO_3$ film for wireless LAN system using TV white space," *2014 IEEE International Ultrasonics Symposium*, Chicago, IL, USA, 2014, pp. 803-806.

27 K. -y. Hashimoto, S. Tanaka and M. Esashi, Tunable RF SAW/BAW filters: Dream or reality?, *2011 Joint Conference of the IEEE International Frequency Control and the European Frequency and Time Forum (FCS) Proceedings*, San Francisco, CA, USA, 2011, pp. 1-8.

28 F. Balteanu, H. Modi, Y. Choi, J. Lee, S. Drogi and S. Khesbak, "5G RF Front End Module Architectures for Mobile Applications," *2019 49th European Microwave Conference (EuMC)*, Paris, France, 2019, pp. 252-255.

29 M. Ramezani, M. Ghatge and R. Tabrizian, High $k_t^2.Q$ silicon Fin Bulk Acoustic Resonators (FinBAR) FOR chip-scale multi-band spectrum analysis, *2018 IEEE Micro Electro Mechanical Systems (MEMS)*, Belfast, UK, 2018, pp. 158-161.

30 J. Anderson, Y. He, B. Bahr, D. Weinstein, Integrated acoustic resonators in commercial fin field-effect transistor technology, *Nature Electronics*, **5**, 611–619 (2022).

31 F. Hakim, T. Tharpe, R. Tabrizian, Ferroelectric-on-Si Super-High-Frequency Fin Bulk Acoustic Resonators With $Hf_{0.5}Zr_{0.5}O_2$ Nanolaminated Transducers, *IEEE Microwave and Wireless Components Letters*, **31**, 701-704 (2021).

32 M. Ghatge, G. Walters, T. Nishida, R. Tabrizian, An ultrathin integrated nanoelectromechanical transducer based on hafnium zirconium oxide, *Nature Electronics*, **2**, 506-512 (2019).

33 He, Y., Bahr, B., Si, M., Ye, P. & Weinstein, D. A tunable ferroelectric based unreleased RF resonator. *Microsyst. Nanoeng.* **6**, 8 (2020).

34 T. Tharpe, E. Hershkovitz, F. Hakim, H. Kim, and R. Tabrizian, Nanoelectromechanical resonators for gigahertz frequency control based on hafnia–zirconia–alumina superlattices, *Nat Electron* **6**, 599–609 (2023).

35 J. Zou, C. M. Lin, C. S. Lam, A. P. Pisano, Transducer design for AlN Lamb wave resonators, Journal of Applied Physics, 121(15), 154502.

36 S. S. Cheema, N. Shanker, LC. Wang, et al. Ultrathin ferroic HfO_2–ZrO_2 superlattice gate stack for advanced transistors, *Nature*, **604**, 65–71 (2022).

37 X. Zheng, T. Tharpe, S. M. E. H. Yousuf, N. G. Rudawski, P. X-L. Feng, R. Tabrizian, High Quality Factors in Superlattice Ferroelectric $Hf_{0.5}Zr_{0.5}O_2$ Nanoelectromechanical Resonators, *ACS Applied Materials & Interfaces,* **14**, 36807-36814 (2022).

38 S. Ghaffari, S. Chandorkar, S. Wang, E. J. Ng, C. H. Ahn, V. Hong, Y. Yang, T. W. Kenny, Quantum Limit of Quality Factor in Silicon Micro and Nano Mechanical Resonators, *Sci Rep*, **3**, 3244 (2013).

39 R. Tabrizian, M. Rais-Zadeh, F. Ayazi, Effect of phonon interactions on limiting the f.Q product of micromechanical resonators, *2009 International Solid-State Sensors, Actuators and Microsystems Conference*, 2009, 2131-2134.

40 F. Hakim, M. Ghatge, R. Tabrizian, Excitation of high-frequency in-plane bulk acoustic resonance modes in geometrically engineered hafnium zirconium oxide nano-electro-mechanical membrane, *Applied Physics Letters*, **117** (6), 2020.

41 R. Abdolvand and F. Ayazi, Enhanced Power Handling and Quality Factor in Thin-Film Piezoelectric-on-Substrate Resonators, *2007 IEEE Ultrasonics Symposium Proceedings*, New York, NY, USA, 2007, pp. 608-611.

42 M. Ghatge, P. Karri, R. Tabrizian, Power-insensitive silicon crystal-cut for amplitude-stable frequency synthesis, *2017 IEEE 30th International Conference on Micro Electro Mechanical Systems (MEMS)*, Las Vegas, NV, USA, 2017, pp. 76-79.

43 R. Ruby, Review and Comparison of Bulk Acoustic Wave FBAR, SMR Technology, *2007 IEEE Ultrasonics Symposium Proceedings*, New York, NY, USA, 2007.

44 J.M.L. Miller, A. Ansari, D. B. Heinz, Y. Chen, I. B. Flader, D. D. Shin, L. G. Villanueva, T. W. Kenny, Effective quality factor tuning mechanisms in micromechanical resonators, *Appllied Physics Review*, **5**, 041307 (2018).

45 T. N. Tanskaya, V. N. Zima, A. G. Kozlov, The influence of surface roughness of Bragg reflector layers on characteristics of microwave solidly mounted resonator, *2015 International Siberian Conference on Control and Communications (SIBCON)*, **2015** 1-4.

46 A. Vorobiev, S. Gevorgian, M. Löffler, E. Olsson, Correlations between microstructure and Q-factor of tunable thin film bulk acoustic wave resonators, *Journal of Applied Physics*, **110**, 054102 (2011).

47 M. Ramezani, V. V. Felmetsger, N. G. Rudawski, R. Tabrizian, Growth of C-Axis Textured AlN Films on Vertical Sidewalls of Silicon Microfins, *Transactions on Ultrasonics, Ferroelectrics, and Frequency Control*, **68**, 753-759 (2021).

48 F. Martin, M. E. Jan, S. Rey-Mermet, B. Belgacem, D. Su, M. Cantoni, P. Muralt, Shear mode coupling and tilted grain growth of AlN thin films in BAW resonators, *IEEE Transactions on Ultrasonics, Ferroelectrics, and Frequency Control*, **53**, 1339-1343 (2006).

49 M. Ramezani, V. V. Felmetsger, N. G. Rudawski, R. Tabrizian, Growth of C-Axis Textured AlN Films on Vertical Sidewalls of Silicon Microfins, *IEEE Transactions on Ultrasonics, Ferroelectrics, and Frequency Control*, vol. **68**, no. 3, pp. 753-759, March 2021.

50 T. Tharpe, X. Q. Zheng, P. X. L. Feng, R. Tabrizian, Resolving Mechanical Properties and Morphology Evolution of Free-Standing Ferroelectric $Hf_{0.5}Zr_{0.5}O_2$, *Advanced Engineering Materials*, **23**, 2101221 (2021).

51 S. S. Fields, D. H. Olson, S. T. Jaszewski, C. M. Fancher, S. W. Smith, D. A. Dickie, G. Esteves, M. D. Henry, P. S. Davids, P. E. Hopkins, J. F.; Ihlefeld, Compositional and phase dependence of elastic modulus of crystalline and amorphous $Hf_{1-x}Zr_xO_2$ thin films, *Appl. Phys. Lett*. **118**, 102901 (2021).

52 C. Mart, T. Kämpfe, R. Hoffmann, S. Eßlinger, S. Kirbach, K. Kühnel, M. Czernohorsky, L. M. Eng, W. Weinreich, Piezoelectric Response of Polycrystalline Silicon-Doped Hafnium Oxide Thin Films Determined by Rapid Temperature Cycles, *Advanced Electronic Materials*, **6**, 1901015 (2020).

53 T. S. Mikolajick, S. Slesazeck, H. Mulaosmanovic, M. H. Park, S. Fichtner, P. Lomenzo, M. Hoffmann, U. Schroeder, Next generation ferroelectric materials for semiconductor process integration and their applications, *Journal of Applied Physics*, **129**, 100901 (2021).

54 D. A. Feld, R. Parker, R. Ruby, P. Bradley and S. Dong, After 60 years: A new formula for computing quality factor is warranted, *2008 IEEE Ultrasonics Symposium*, Beijing, China, 2008, pp. 431-436.

55 R. Lu, M. -H. Li, Y. Yang, T. Manzaneque and S. Gong, Accurate Extraction of Large Electromechanical Coupling in Piezoelectric MEMS Resonators, *Journal of Microelectromechanical Systems*, vol. **28**, no. 2, pp. 209-218, April 2019.

56 O. J. Zobel, Theory and Design of Uniform and Composite Electric Wave Filters, *The Bell System Technical Journal*, **2**, 1-46 (1923).

57 D. Psychogiou, R. Gómez-García, D. Peroulis, Single and Multiband Acoustic-Wave-Lumped- Element-Resonator (AWLR) Bandpass Filters With Reconfigurable Transfer Function, *IEEE Transactions on Microwave Theory and Techniques*, vol. **64**, no. 12, pp. 4394-4404, Dec. 2016.

58 A. Gao, K. Liu, J. Liang, T. Wu, AlN MEMS filters with extremely high bandwidth widening capability, Microsystems & Nanoengineering, **6**, 74 (2020).

59 M. Ghatge, R. Tabrizian, Dispersion-Engineered Guided-Wave Resonators in Anisotropic Single-Crystal Substrates—Part I: Concept and Analytical Design, *IEEE Transactions on Ultrasonics, Ferroelectrics, and Frequency Control*, **66**, 1140-1148 (2019).

60 M. Ghatge, M. Ramezani and R. Tabrizian, Dispersion-Engineered Guided-Wave Resonators in Anisotropic Single-Crystal Substrates—Part II: Numerical and Experimental Characterization, *IEEE Transactions on Ultrasonics, Ferroelectrics, and Frequency Control*, **66**, 1149-1154 (2019).

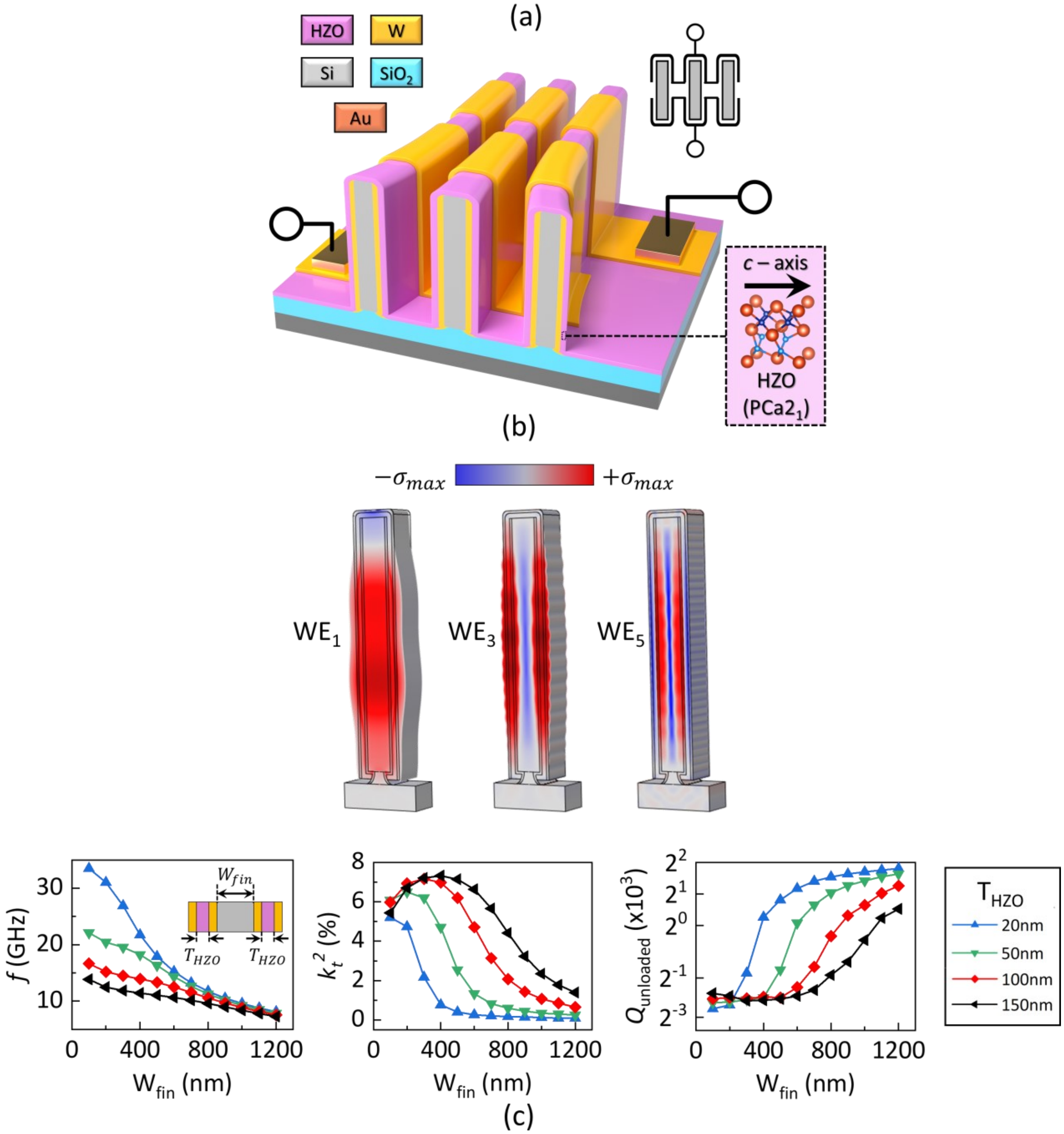

Figure 1. Ferroelectric-gate fin (FGF) nano-acoustic resonator concept and scaling characteristics. (a) Schematic demonstration of FGF resonator created from three parallel fins. The resonator relies on two three-dimensional gates that are electrically coupled through the ferroelectric HZO transducer and bottom floating W electrodes. The left inset shows proposed symbol for the one-port device. (b) COMSOL-simulated mode-shapes for FGF resonator operating in width-extensional bulk acoustic wave modes with odd harmonics of 1, 3, and 5. (c) Analytically modeled frequency, Q, and k_t^2 scaling characteristics of FGF resonators for different Si fin width and HZO transducer thicknesses.

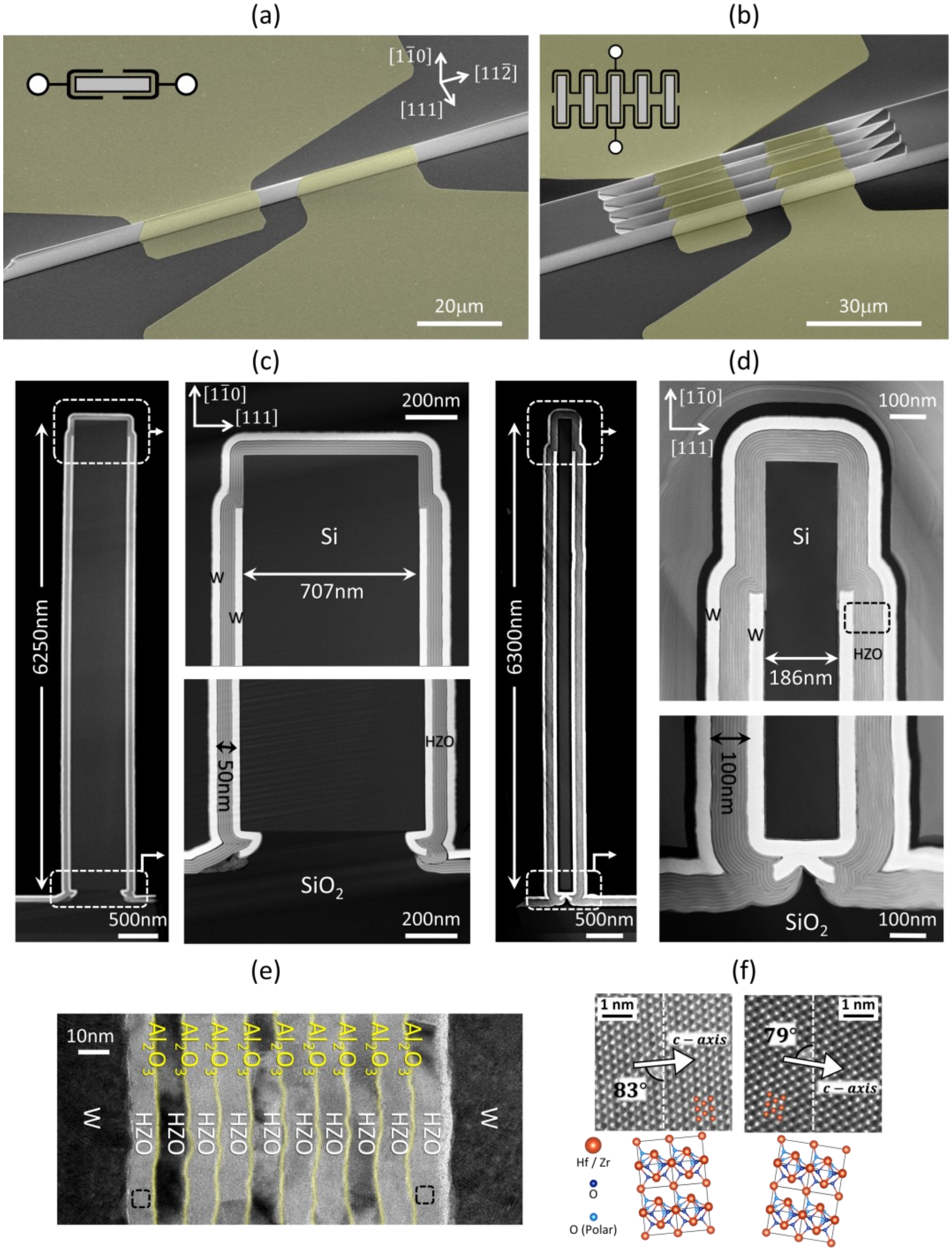

Figure 2. Three-dimensional and cross-sectional images of ferroelectric-gate fin acoustic resonators. SEM image of FGF resonator with (a) single fin and (b) five parallel fins. HAADF-STEM image FGF resonators with (c) 707nm Si fin width and (d) 186nm Si fin width, and aspect ratio exceeding 34:1. Zoomed-in images at top and bottom corners of FGF resonators are also shown, highlighting three-dimensional patterning of W electrodes and conformal coverage of HZO transducer. (e) HR-TEM image of HZO superlattice transducer, highlighting alumina interlayers that are used to sustain polar orthorhombic phase with large piezoelectricity. (f) HAADF-STEM images obtained from the selected areas in HZO transducer and their reconstructed atomic structure highlighting *c*-axis orientation.

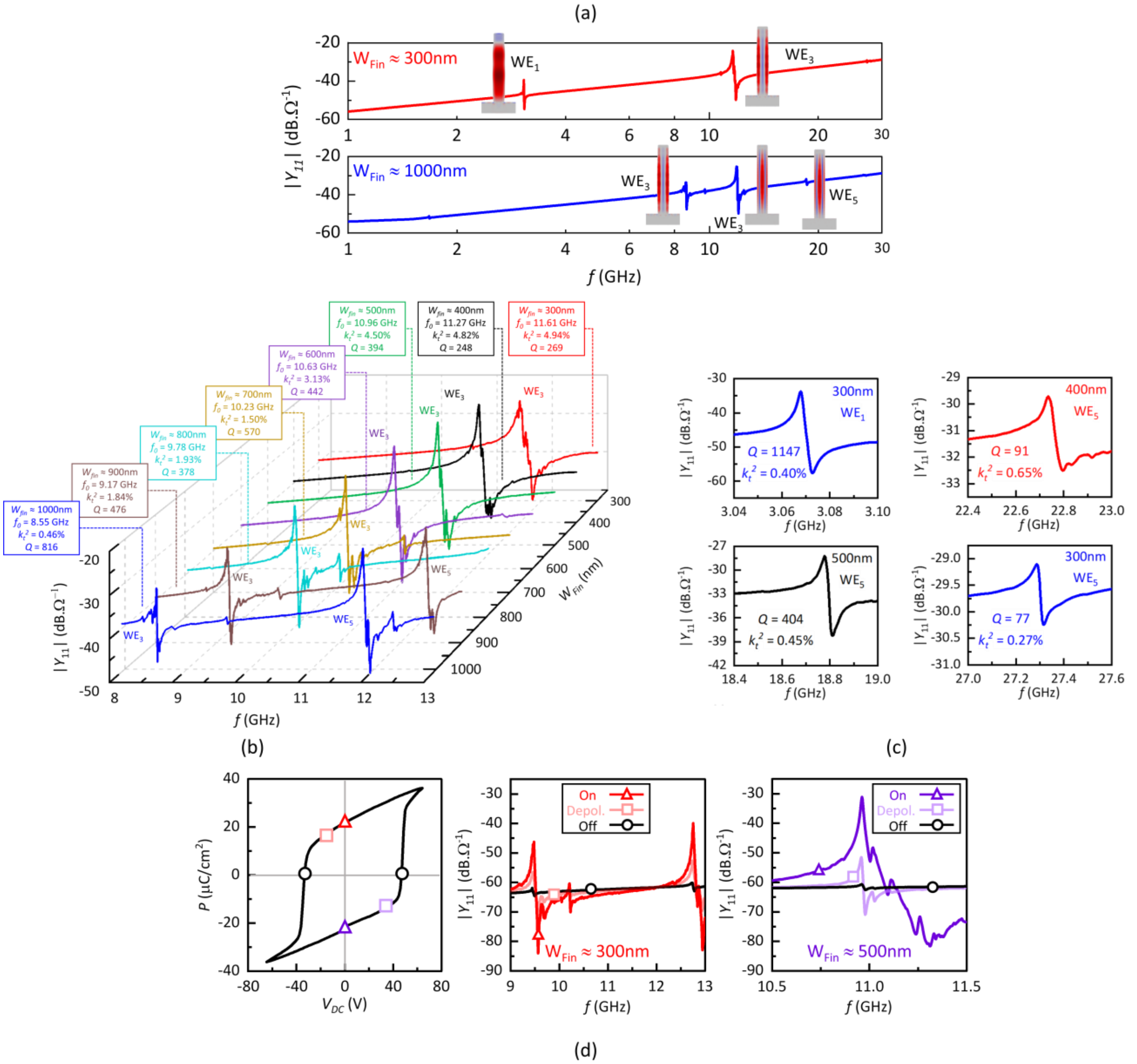

Figure 3. Measured admittance of intrinsically switchable FGF nano-acoustic resonators. (a) Large-span admittance for FGF resonators with fin width of 1000nm and 300nm, highlighting various width-extensional harmonics over 3-30 GHz. (b) Admittance of resonators close to WE_3 mode, for fin widths over 300nm to 1000nm. (c) Small-span admittance for various harmonic peaks over 18-30 GHz. The fin width and WE modes are noted for each admittance plot. (d) Intrinsic switching characteristic of FGF resonators with fin widths of 300nm and 500nm. The admittance transformation from On state to Off state is shown.

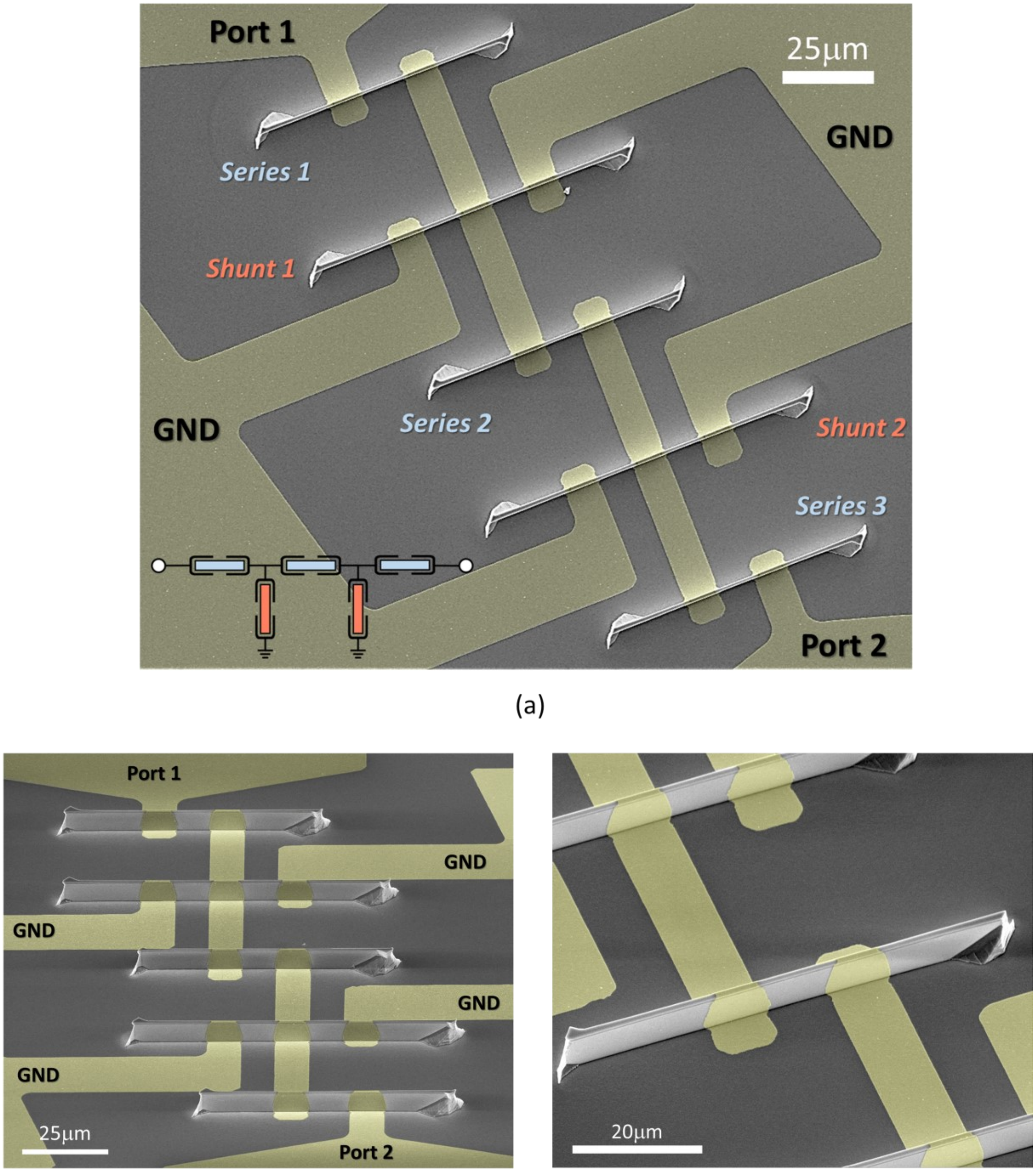

(a)

(b)

(c)

Figure 4. Images of implemented FGF filter array. (a) SEM image of FGF filter array to cover 9-12 GHz with lithographically tailorable center-frequencies and bandwidths. (b) Side-view of FGF filters created from five resonators connected in 2.5-stage ladder configuration. The series and shunt elements creating the ladder filter, highlighted in SEM image, are connected through planar routings. (c) Zoomed-in SEM image of filter around a three-dimensional gate on a series element, showing a slight taper across fin height. This is due to the slightly different exposure dose on piezoelectric mask across fin height.

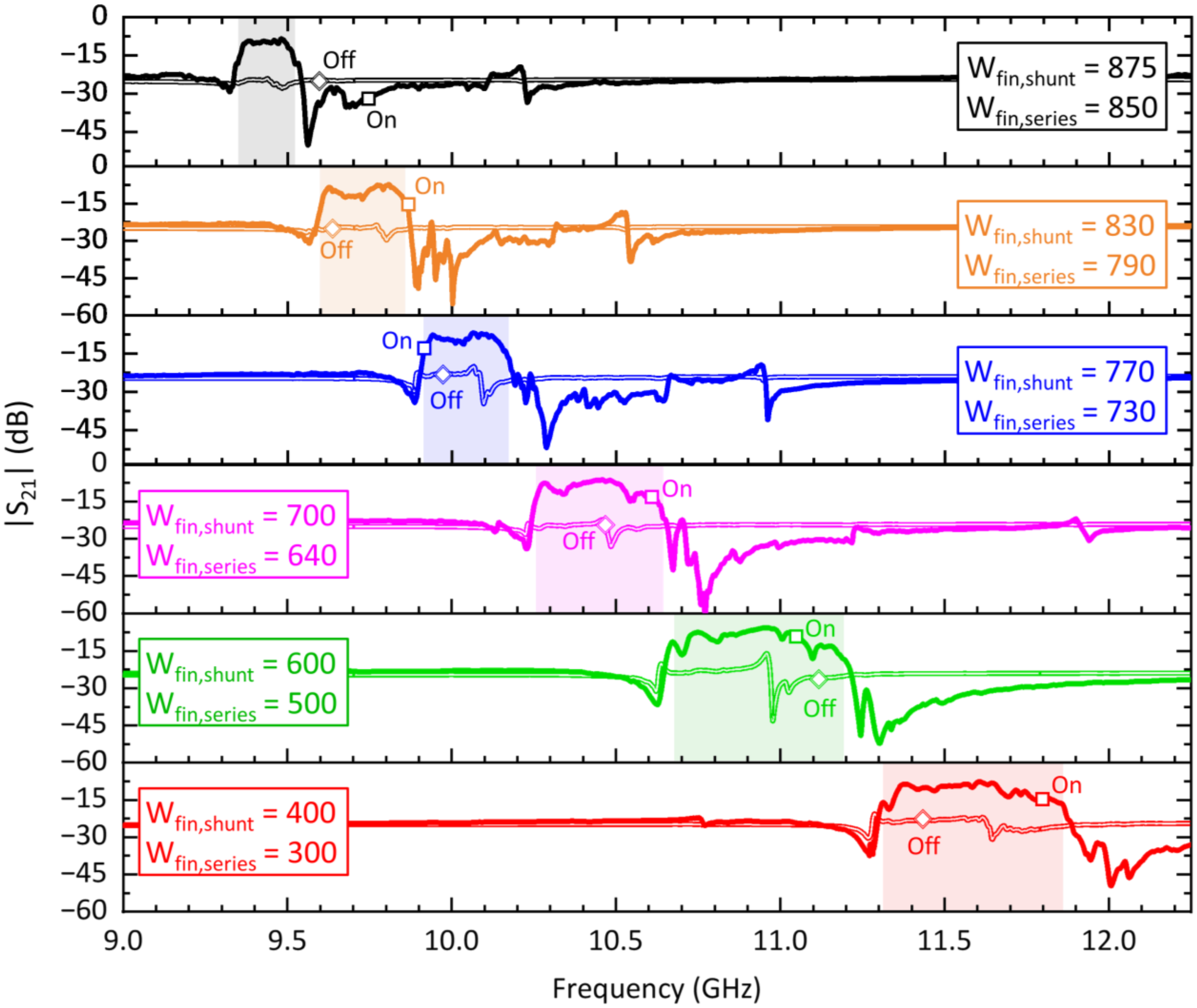

Figure 5. Measured transmission response of intrinsically switchable FGF filter array. $|S_{21}|$ of six filters created from FGF resonators with different fin widths, covering 9-12 GHz. Each filter is created from FGFs with slightly different fin widths to enable formation of highly-selective passband when resonators are coupled in ladder configuration. The approximate fin width of resonators for each filter is shown in legend. For each FGF filter, the transmission response is shown in both of On and Off states.